Finite element modelling for electrical discharge machining of Ti-6Al-4V alloy and multi-objective optimisation using response surface modelling

Diksha Jaurker, Mohan Kumar Pradhan

Finite element modelling for electrical discharge machining of Ti-6Al-4V alloy and multi-objective optimisation using response surface modelling

Diksha Jaurker

Department of Mechanical Engineering,
Maulana Azad National Institute of Technology,
Bhopal, India
Email: dikshajaurker17@gmail.com

Mohan Kumar Pradhan*

Department of Mechanical Engineering,
National Institute of Technology,
Raipur, India
Email: mkpradhan.me@nitrr.ac.in
Email: mohanrkl@gmail.com
*Corresponding author

Abstract: Electrical discharge machining (EDM) is a non-traditional precision machining method that thermally erodes hard materials and complicated geometries with excellent accuracy, but it also creates residual stress and fractures. Finite element modelling (FEM) was performed for an axially symmetric two-dimensional model of the EDM method, taking into account plausible factors such as Gaussian heat flux distribution, thermally sensitive material properties, the proportion of heat distribution to the workpiece, plasma flushing efficiency (PFE), and so on, to assess the consequence of process variables on the temperature field during the heating stage, and then material removal rate (MRR) and residual stresses. Utilising the response surface modelling (RSM) approach, multi-objective optimisation was performed to maximise the MRR and minimise tensile residual stresses, and an optimum solution was found by assigning equal weightage to all objective functions.

Keywords: electrical discharge machining; EDM; finite element method; simulation modelling; response surface methodology.

Biographical notes: Diksha Jaurker was a MTech Scholar in the Department of Mechanical Engineering, Maulana Azad National Institute of Technology, Bhopal, India and currently pursuing PhD at the Indian Institute Technology Indore.

Mohan Kumar Pradhan is an Associate Professor of Mechanical Engineering at the National Institute of Technology, Raipur, and a Former Assistant Professor (G-1) in MANIT, Bhopal. He received his MTech and PhD from the National Institute of Technology, Rourkela, India. He has advised over 80 graduates, 42 post-graduates, and four PhD students, and is currently advising five PhD students. His research interests include various aspects of machining, process modelling, and optimisation. He has authored over 160 refereed publications, one book, 25 book chapters and edited two books, five conference proceedings, and five journals as a guest editor. He was featured in the list of top 2% scientists worldwide in 2021 and 2022, compiled by a team of scientists from Stanford University in the USA. He is a charted engineer, a Life Fellow of IIPE and life member of ISTE, IACSIT, IAENG and MIE (I).

1 Introduction

Electrical discharge machining (EDM) is an attractive non-traditional electrically conductive material process acquiring interest for a NIL force, non-contact process with the potential of governing the process parameters to achieve the required surface finish and dimensional accuracy. It has gained enormous prominence in industries such

as aerospace, automotive, die industries, mould making, medical, micro-mechanics, electronics industry, and so on (Jaurker and Pradhan, 2022; Nayak et al., 2022). It does, though, have a few disadvantages, such as limited machining efficiency and compromised surface quality due to induced residual stresses. To address these restrictions, a number of initiatives have been undertaken to acquire a more material removal rate (MRR) and lower tensile residual stresses (Pradhan and Biswas, 2010).

Recently, many researchers have studied different expects of EDM (Tang and Yang, 2018) have done simulation study on residual stress and thermal phase transformation EDM of Ti-6Al-4V, and have performed ANOVA analysis. They stated that the maximum tensile stress is more closely related to the I, and the T_{on} has a higher impact on the depth position of the maximum tensile stress. As a result, increasing the discharge energy causes cracks to grow to a greater depth. Joshi and Pande (2010) had developed a thermo-physical model for die-sinking EDM, and they found that the crater depth was shown to be highly affected by I and V, whereas the key influencing process factors were T_{on} and I for the MRR. They had validated these results with experimental results. Pradhan and Bhattacharyya (2009) studied micro-EDM of Ti-6Al-4V and optimised the process using response surface modelling (RSM) and artificial neural network (ANN) and found that the model's predicted optimum values were very close to the experimental values. Gu et al. (2012) investigated Ti-6Al-4V EDM process with a bundled die-sinking electrode, and found that the bundled electrodes sustain far more current I than solid electrodes, resulting in a lower tool wear and MRR is shown to be significantly affected by fluid flow rate, I, and the interplay between T_{on} and I. Mhatre et al. (2014) analysed EDM of Ti-6Al-4V and found that the peak value of I is the main important parameter for MRR, drilled hole surface integrity, and dimensional accuracy. Pradhan and Biswas (2008) studied thermal distribution and thermal stresses. According to their findings, tensile residual stresses accumulate along the crater border in all different directions throughout the EDM process. The tensile residual strains in the material are minor after a single heat flux, however, they can accumulate during multiple spark cycles, resulting in surface damage like micro-cracks. Pradhan (2012) suggested a fusion of RSM, grey relational analysis (GRA), and principal component analysis (PCA) modelling along with an optimisation method for determining the optimal process parameters that maximise MRR without impacting surface quality in EDM of an AISI D2 tool steel (Pradhan et al., 2018) provides another hybrid, integrated technique of GRA coupled with Shannon's entropy weighted TOPSIS method for optimising EDM machining settings, and discovers that I is the most critical process parameter. Yadava et al. (2004) analysed electro-discharge diamond grinding (EDDG), The results show that thermal stresses are larger close to the top surface at first but move away from the top after certain time of grinding. Kansal et al. (2008) create the finite element modelling (FEM) model for powder mixed EDM and analyse the temperature

profile and MRR by studying temperature profiles, and discovered that several various process factors impact the temperature profile throughout the depth and radius of the workpiece. Jithin et al. (2020) performed surface roughness prediction after EDM considering cathode energy fraction, as well as plasma flushing efficiency (PFE). Ming et al. (2022) reviewed the material removal mechanisms, machining process simulations, and machining performance assessments for the molecular dynamic models applied to the EDM process. A comparison is made between FEM, MD, and flow field models, along with the relevant research areas that might be supported in the future. Shastri and Mohanty (2022) studied the surface properties of the Nimonic C263 workpiece while it was being machined with three different, regularly used EDM tools: copper-tungsten, tungsten, and copper.

In the current investigation, a FEM model has been made to determine the effect of I, T_{on} and V on MRR, residual stresses, while also considering the effect of PFE which is a function of I and T_{on}. And the process has been optimised using RSM.

2   Mechanism of EDM

The process of EDM involves an electrically conductive workpiece and tool, submerged in dielectric fluid. A high voltage is delivered over two electrodes immersed in a dielectric fluid with no physical contact between them; no current flows across them. When the tool is brought near to the workpiece, increasing the electric field causes a breakdown of the dielectric fluid's electrical resistance and alters its behaviour from insulator to conductor at these points, resulting in the spark (Pradhan and Biswas, 2008b, 2009). As a result, material is eroded from the workpiece by regional melting. The current then continues to pass, and the continued attacks of electrons and ions on the electrodes generate extreme heating of the workpiece material, culminating in a temperature rise of up to 12,000°C (Boothroyd and Winston, 1989; Pradhan and Patel, 2020). As a result, a small molten metal pool forms at the area of both electrodes, from which certain metal portions are immediately vaporised. As the plasma channel increases during the discharge, the radius of the molten metal pool also expands. As the discharge ends, current and voltage are cut off, forcing the plasma to erupt under the pressure created by the encircling dielectric fluid and causing the molten metal pool to be violently pushed together with the dielectric, forming a tiny crater on the workpiece surface.

3   Finite element modelling

The domain is represented as a 2D semi-infinite object for the single discharge. The processing face is the cylinder's top surface, and the ionised stream is focused on its axis. A Gaussian heat flux distribution is considered. When a spark impinges on the workpiece, symmetric heat dispersion

occurs in all directions, and thus a cylindrically formed segment of the workpiece falling inside the spark is designated as the domain, and looking at the 2D plane, it is a rectangular area. The pulse power supplies each spark produces causes heat to be created (Bhiradi et al., 2019; Mohanty et al., 2017; Pradhan and Biswas, 2008). EDM sparks are bell-shaped, having a substantially larger radius near the workpiece, than the radius closer to the tool, as the strong internal plasma pressure pushes back the high-density dielectric that is changing into plasma at the junction. The radius of plasma rises with time, while the mass or radius of the spark is zero at zero time (Eubank et al., 1993). This postulated equation was modified as a function of pulse-on duration and discharge current by utilising single spark encounter's experimental results for the radius of the hole to construct the empirical connection known as the equivalent heat input radius, mentioned in equation (1).

$$R_s = 2,040 \ I^{0.43} \ T_{on}^{0.44} \tag{1}$$

The crater dimensions created through experiments will be lesser than the theoretically calculated crater dimensions. This is due to inefficient molten material flushing, which results in molten material re-solidification. Hence considering the value of PFE is important, which is expressed as the ratio of actual crater volume created for every pulse to theoretical crater volume. The expression for PFE which is used in this study is predicted by Jithin et al. (2017), and it is expressed in equation (2):

$$\begin{aligned} PFE = {} & 0.1093 + (2.238 \times 10^{-2} \times I) \\ & - (8.441 \times 10^{-4} \times t_{on}) \\ & - (4.67 \times 10^{-5} \times I \times T_{on}) \\ & + (4.912 \times 10^{-6} \times T_{on}^2) \end{aligned} \tag{2}$$

So, the Gaussian heat flux distribution can be expressed as mentioned in equation (3):

$$q_w(r) = PFE \frac{4.45 P_w U I}{\pi R_s^2} \exp\left\{-4.5 \left(\frac{r}{R_s}\right)^2\right\} \tag{3}$$

Assumptions for this study:

1 The domain was axisymmetric.

2 The workpiece material was isotropic and homogenous.

3 The ambient temperature was room temperature.

4 The workpiece had linear material behaviour before yielding and elastic-perfectly plastic material behaviour after yielding.

5 The workpiece material's thermal properties are temperature dependent.

6 The convective heat transfer takes place on the workpiece surface.

7 The spark heat input follows a Gaussian heat flux distribution.

8 The workpiece is stress-free initially.

9 The shape of element is not affected due to thermal expansion.

The modelling and simulation were done using ANSYS APDL Software 2021R2 (ANSYS, 2011). The workpiece was a square 2D body, where the length of the edge of the workpiece was considered to be six times the R_s, 'PLANE 13' coupled field solid quadrilateral element defined by four nodes with up to four degrees of freedom per node, capable of reflecting thermo-structural features. On the workpiece, non-uniformly spread mapping meshing with quadrilateral-shaped components was performed. That was finer in the region where heat input is delivered and got coarser as one moves away from the heat source. An initial mesh was generated and results were calculated, then a finer mesh was analysed until there was very little difference between the results obtained from the successive meshes. In the final mesh, there are 19,200 elements and 19,441 nodes in the mesh, which is shown in Figure 1.

**Figure 1** Mesh generated (see online version for colours)
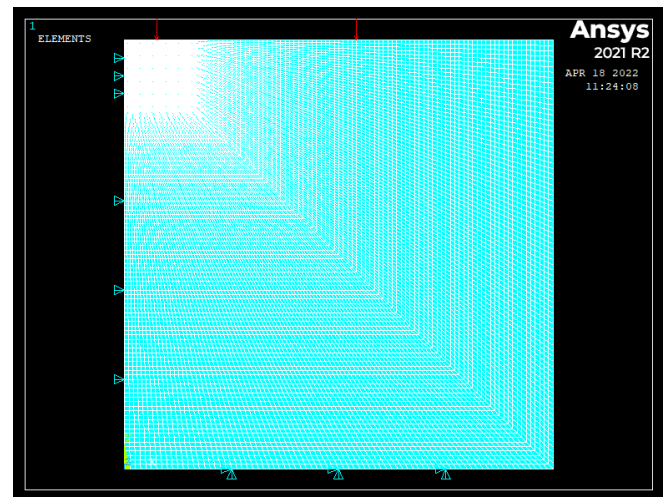
3.1 Boundary conditions

The boundary conditions for the thermal modelling are shown in Figure 2. Throughout the heating phase, the upper surface $\Gamma 1$ is exposed to heat flux with a Gaussian distribution up to R_s, while the remainder of the surface emits heat to the dielectric fluid by convection. During the cooling phase, the whole top surface loses energy to the dielectric via convection heat transfer. Because of the relatively short time-span of the spark, no heat transmission occurs across surfaces $\Gamma 2$ and $\Gamma 3$, which are supposed to be sufficiently distant from the source of heat for heat transfer to occur. And because the axis of symmetry is at $\Gamma 4$, there is no net heat exchange across it.

And structurally, $\Gamma 1$ and $\Gamma 4$ are supposed to have fixed support, i.e., no displacement in the x and y directions takes place.

Figure 2 Boundary conditions (see online version for colours)
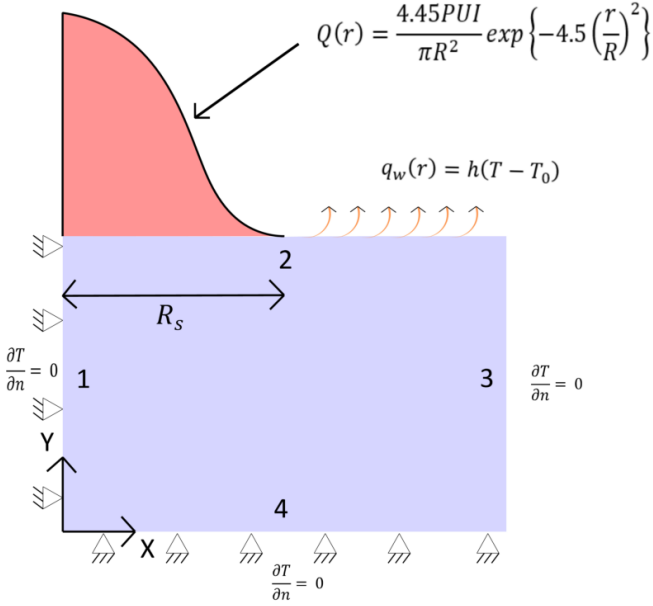
3.1.1 Initial conditions

Originally, the workpiece's temperature is equatable to the ambient temperature.

$$T_{initial} = 298 \text{ K}$$

3.1.2 Boundary conditions during process

- At $\Gamma 1$:

  For $0 < t \leq T_{on}$

  $$q_w(r) = \begin{cases} PFE\frac{4.45P_wUI}{\pi R_s^2} \\ \exp\left\{-4.5\left(\frac{r}{R_s}\right)^2\right\}, & \text{for } r \leq R_s \\ h(T - T_0), & \text{for } r > R_s \end{cases} \quad (4)$$

  For $t > T_{on}$

  $$q_w(r) = h(T - T_0), \text{ for } \forall r \quad (5)$$

- At $\Gamma 2$, $\Gamma 3$ and $\Gamma 4$:

  $$\frac{\partial T}{\partial n} = 0 \quad (6)$$

  where h is coefficient of convective heat transfer between the workpiece and dielectric fluid, T_0 is ambient temperature, and n is the surface's normal direction.

4 Results

4.1 Analysis of MRR and residual stresses using FEM

The data was extracted from the FEM following a full-factorial design of experiment and the results were MRR, RS_r and RS_a for the different combinations of I, T_{on} and V input parameters and the corresponding values of PFE. The temperature distribution on the workpiece just after the end of the heating period is presented in Figure 3, where it can be seen that the maximum temperature of 5,238 K has been attained at that point where the axis of plasma coincides, and gradually the temperature decreases while moving away from that point. The elements having a temperature greater than the melting point of the workpiece material were eliminated and the crater was formed, which is shown in Figure 4. This updated model is used for structural analysis to analyse the residual stresses in radial direction and axial direction which are shown in Figures 5 and 6 respectively, for $I = 6$ A, $T_{on} = 15$ μsec and $V = 120$ V. The FEM model created in this study was validated by previous literature (Choubey et al., 2020).

Figure 3 Temprature distribution on the workpiece just after heating period (see online version for colours)
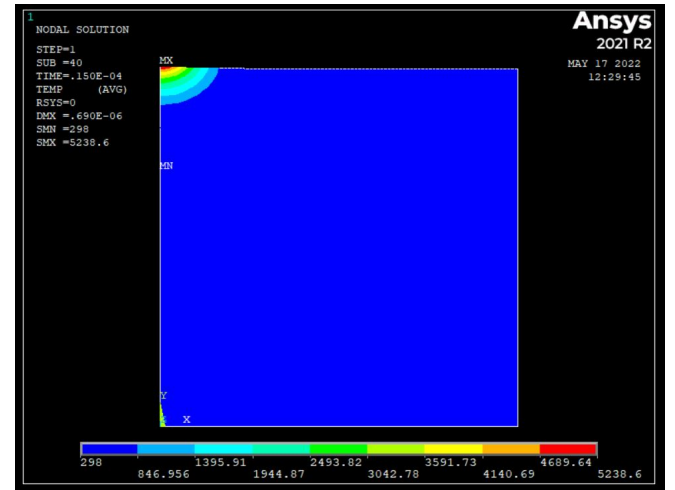
4.2 Mathematical model for MRR and residual stresses

A quadratic model with Akaike's information criterion and backward selection was proposed for the response variables MRR, RS_r and RS_a were evaluated by the F-test of ANOVA. The fit summary reveals that the fitted quadratic model is statistically significant for analysing the response variables. When the R^2 approaches unity, the better the response model fits the actual data using Design-Expert 13, and the data was analysed. Using ANOVA to evaluate the suitability of the constructed models. Further, the value of the signal-to-noise ratio is measured by adequate precision (AP) in this model, which compares the range of the predicted value at the design point to the average prediction error, is well above 4.

For MRR at a 95% confidence level, the model's P-value is 0.05. Table 1 shows the fit statistics, where the predicted R^2 of 0.9840 is within a difference of 0.2 with the adjusted R^2 of 0.9852, indicates statistically significance of the model. The AP of 112.261 suggests a satisfactory signal. The coded factor equation expressed is used to predict the response for each element's varying level. The high and lowest levels of the factors are coded as +1 and –1 by

default, respectively. By comparing the coefficients of the factors, the coded equation can also be used to determine the respective importance of the factors. Where A is I, B is T_{on} and C is V. The coded factor equation for MRR is shown in equation (7).

Table 1 Fit statistics MRR

Std. dev.	1.35E-06	R^2	0.9866
Mean	0	Adjusted R^2	0.9852
CV%	8.51	Predicted R^2	0.984
		Adeq. precision	112.2606

Table 2 Fit statistics radial residual stresses

Std. dev.	58,697.99	R^2	0.6434
Mean	3.81×10^5	Adjusted R^2	0.6077
CV%	15.4	Predicted R^2	0.5667
		Adeq. precision	19.1868

For RS_r at a 95% confidence level, the model's P-value is 0.05. Table 2 shows the fit statistics, where, the predicted R^2 of 0.5667 is within a difference of 0.2 with the adjusted R^2 of 0.6077 and AP of 19.1868 suggests a satisfactory signal. The coded factor equation for RS_r are shown in equation (8).

For RS_r at a 95% confidence level, the model's P-value is 0.05. Table 3 shows the fit statistics, where, the predicted R^2 of 0.7990 is within a difference of 0.2 with the adjusted R^2 of 0.8205 and AP OF 29.6280 suggests a satisfactory signal. The coded factor equation for RS_r are shown in equation (9).

$$
\begin{aligned}
MRR = {} & 1.50489 \times 10^{-5} + 1.3166 \times 10^{-5}A \\
& - 5.83911 \times 10^{-6}B + 4.51372 \times 10^{-6}C \\
& - 3.13752 \times 10^{-6}AB + 2.4009 \times 10^{-6}AC \\
& - 5.89062 \times 10^{-7}BC + 4.76357 \times 10^{-8}A^2 \\
& + 2.57693 \times 10^{-6}B^2 - 9.03022 \times 10^{-7}C^2
\end{aligned} \tag{7}
$$

$$
\begin{aligned}
RS_r = {} & 331{,}770 + 47{,}300.4 \times A + 10{,}219.6 \times B \\
& - 34{,}704.3 \times C - 16{,}778.9 \times AB \\
& - 56{,}192.6 \times AC + 22{,}039.4 \times BC \\
& + 122{,}385 \times A^2 - 7{,}630.03 \times B^2 \\
& - 14{,}218.3 \times C^2
\end{aligned} \tag{8}
$$

$$
\begin{aligned}
RS_a = {} & 446{,}446 + 41{,}262 \times A + 76{,}534.1 \times B \\
& - 103{,}221 \times C - 21{,}268.6 \times AB \\
& + 12{,}132.3 \times AC - 16{,}186.1 \times BC \\
& + 32{,}730.6 \times A^2 - 28{,}239.3 \times B^2 \\
& + 10{,}677.7 \times C^2
\end{aligned} \tag{9}
$$

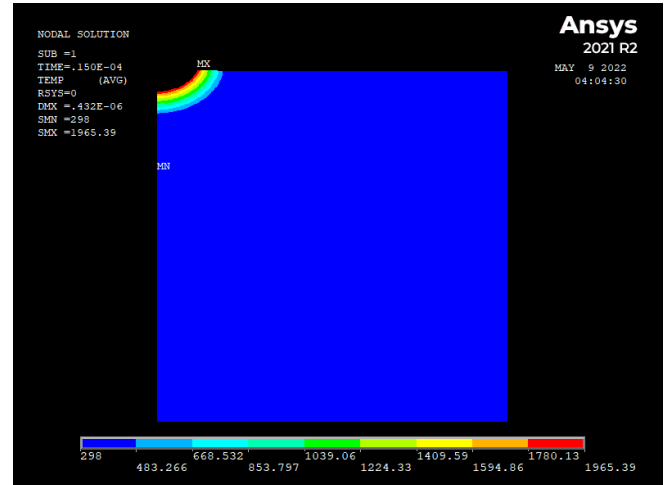**Figure 4** Crater formed (see online version for colours)

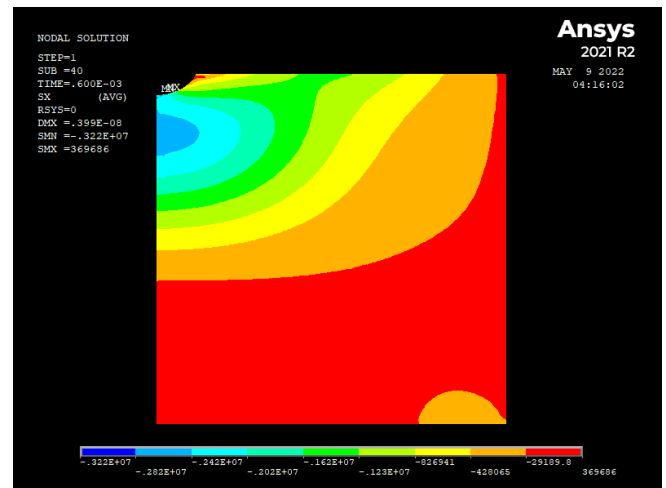**Figure 5** Residual stress in radial direction (see online version for colours)

Figure 6 Residual stress in axial direction (see online version for colours)
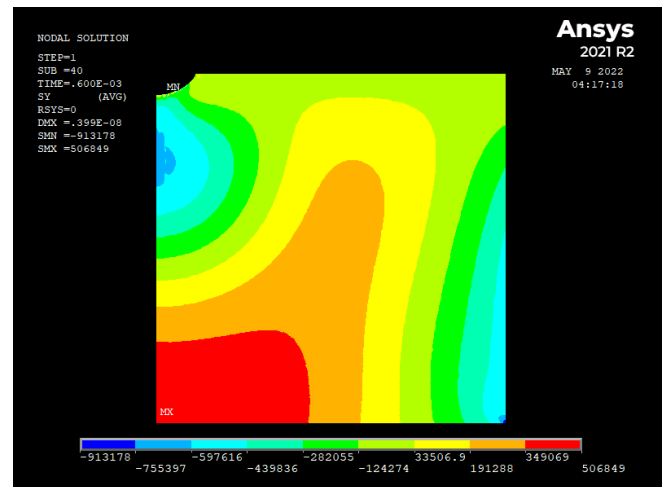
Figure 7   Response surface for MRR with I and T_{on}, (a) V = 90 V (b) V = 180 V (see online version for colours)
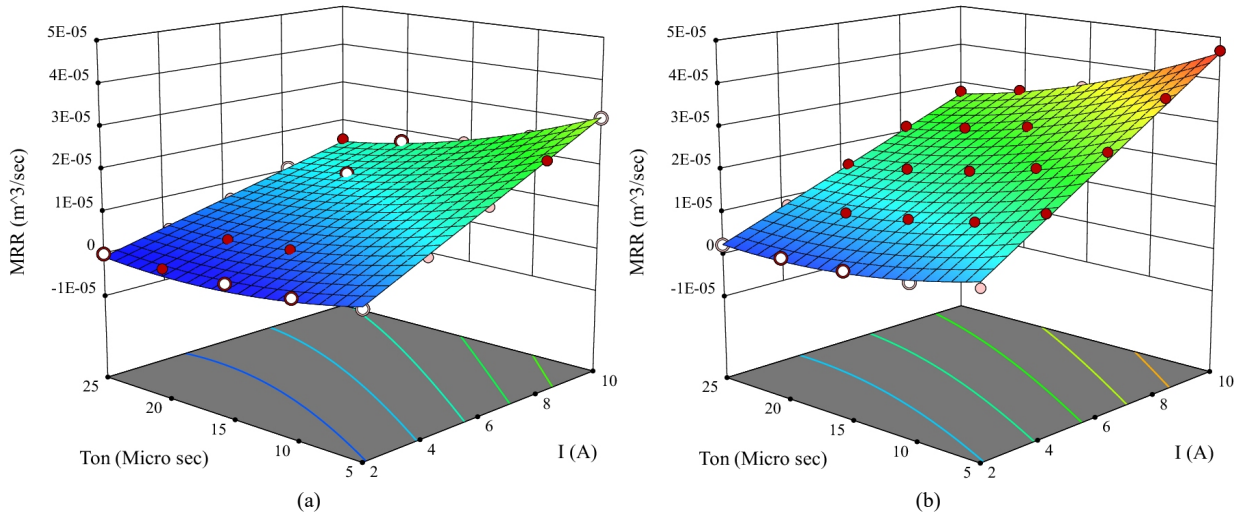

(a)

(b)

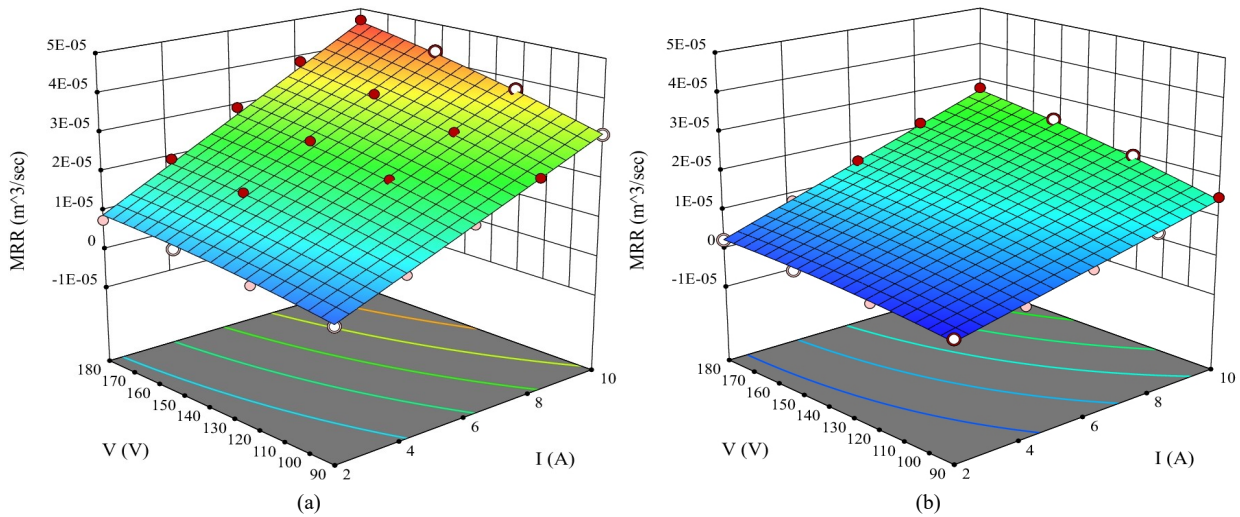**Figure 8**   Response surface for MRR with I and V, (a) T_{on} = 5 (b) T_{on} = 25 (see online version for colours)

(a)

(b)

Figure 9   Response surface for MRR with T and V, (a) I = 2 A (b) I = 10 A (see online version for colours)

(a)

(b)

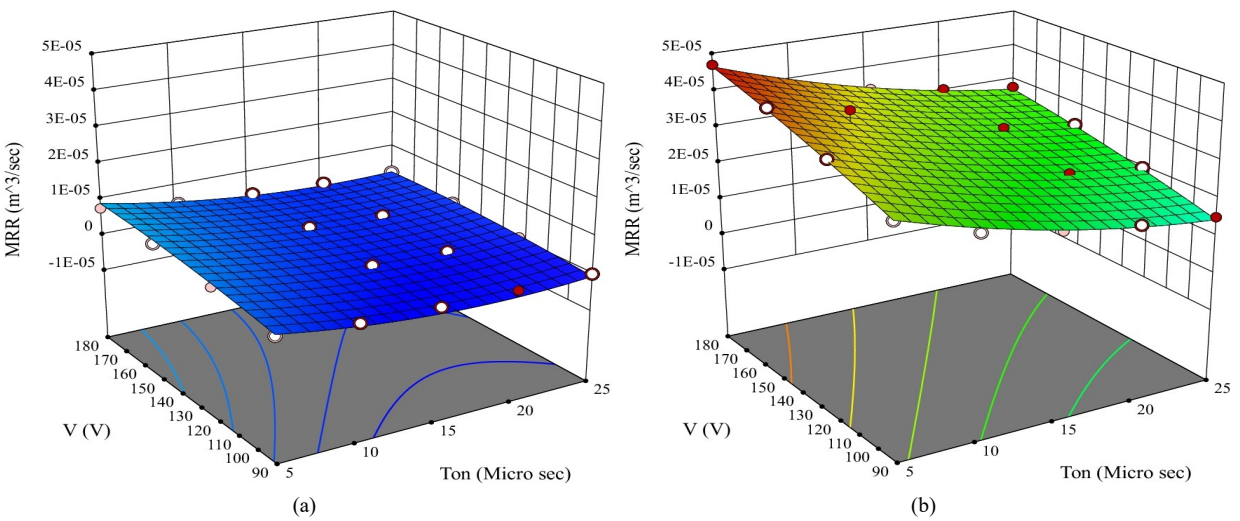**Figure 10**   Response surface for RS_r with I and T_{on}, (a) V = 90 V (b) V = 180 V (see online version for colours)

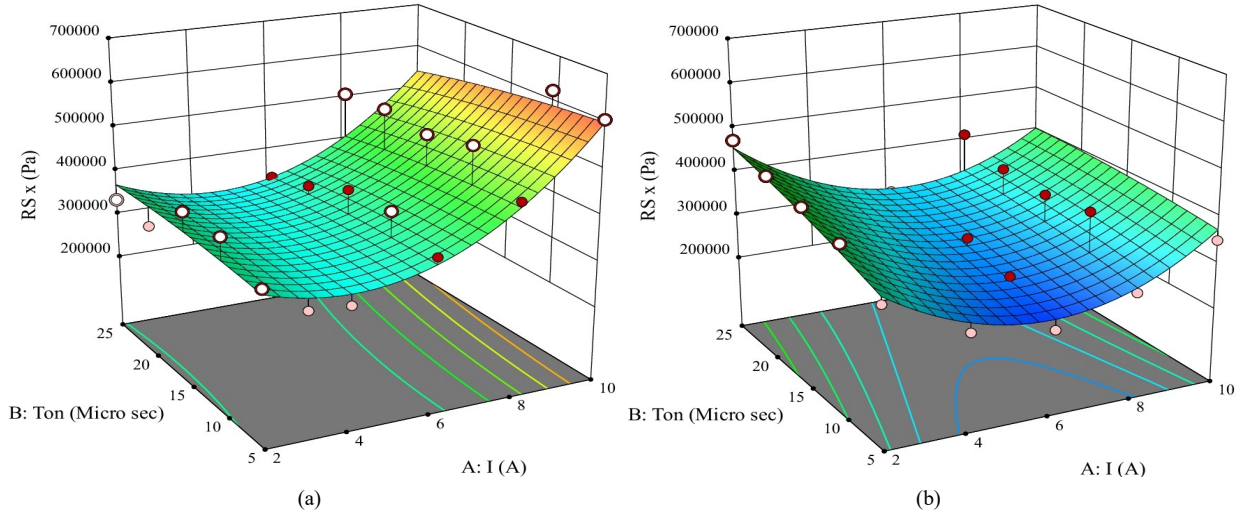(a)   (b)

Figure 11   Response surface for RS_r with I and V, (a) T_{on} = 5 (b) T_{on} = 25 (see online version for colours)
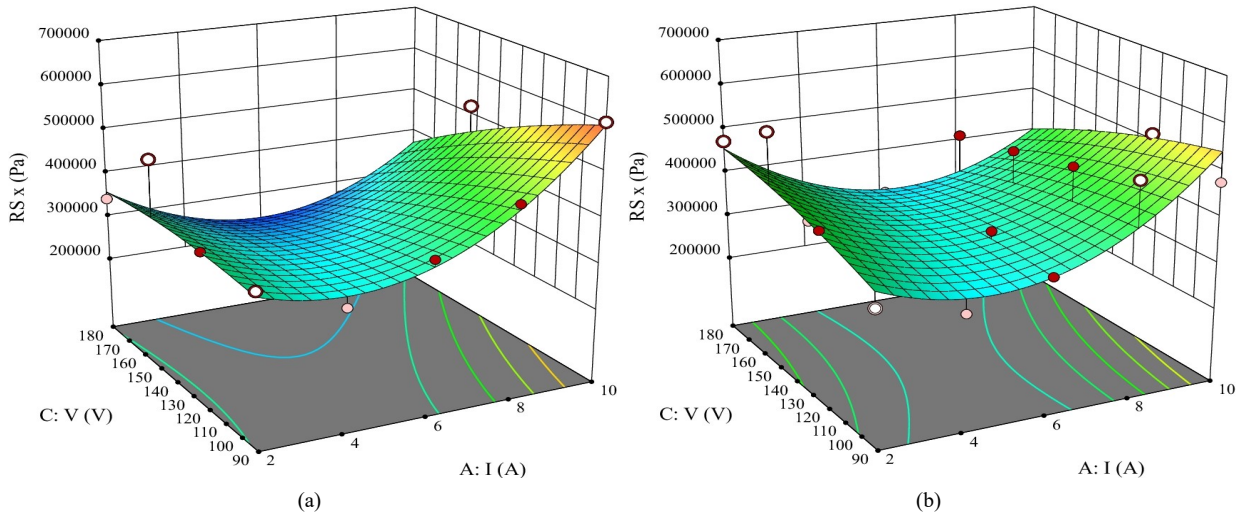

(a)   (b)

Figure 12   Response surface for RS_r with T and V, (a) I = 2 A (b) I = 10 A (see online version for colours)
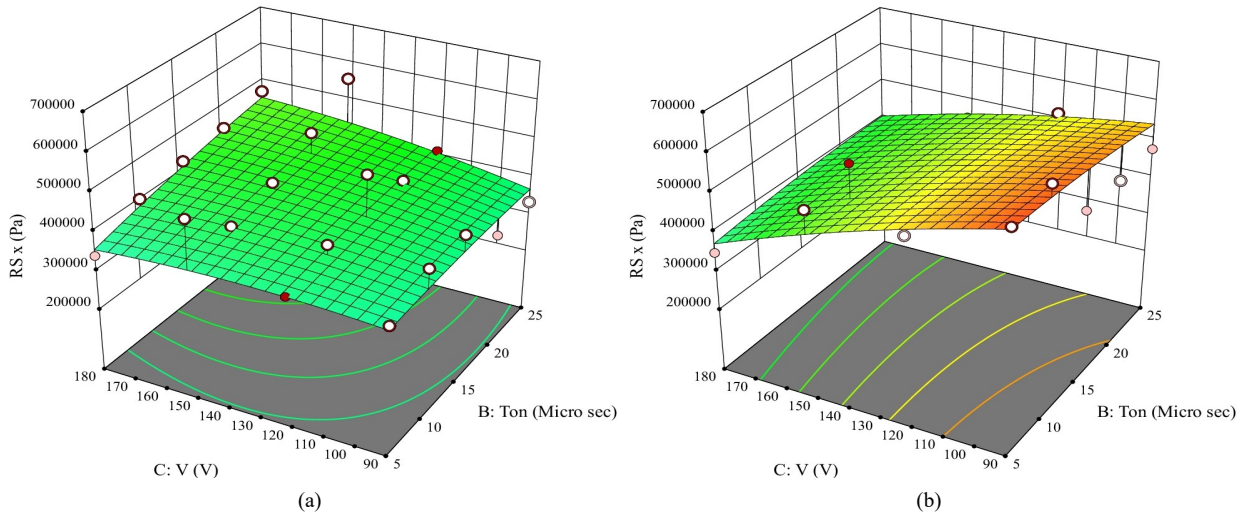

(a)   (b)

Figure 13   Response surface for RS_a with I and T_{on}, (a) V = 90 V (b) V = 180 V (see online version for colours)
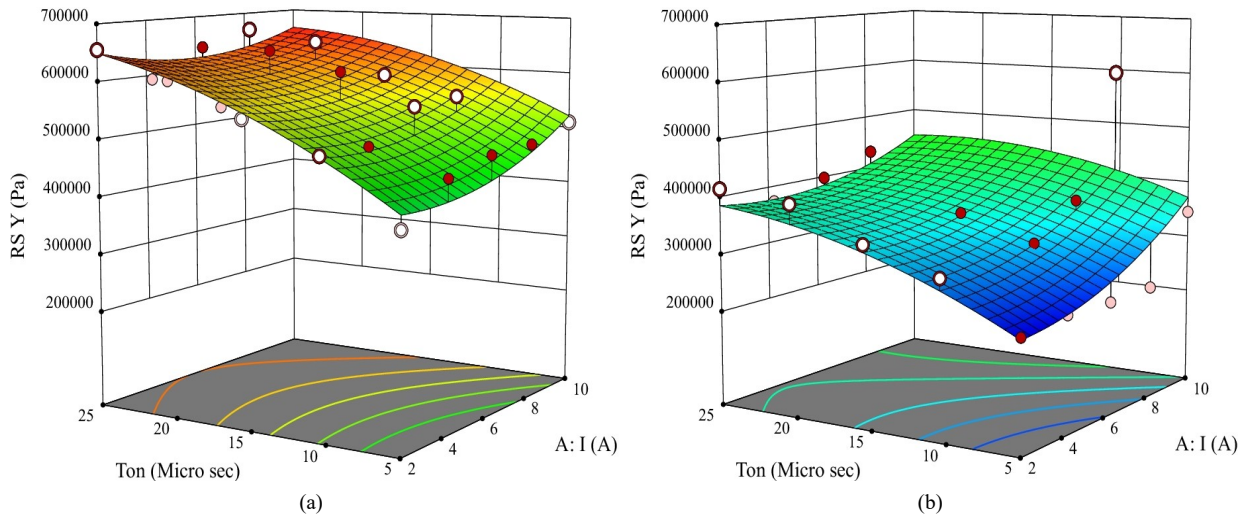

(a)

(b)

Figure 14   Response surface for RS_a with I and V, (a) T_{on} = 5 (b) T_{on} = 25 (see online version for colours)
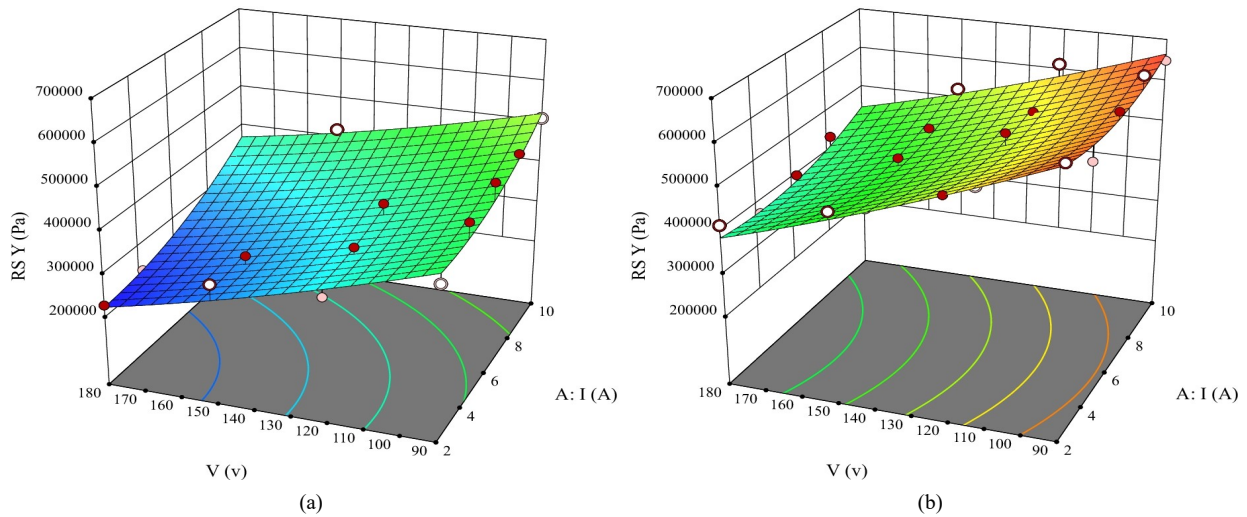

(a)

(b)

Figure 15   Response surface for RS_a with T and V, (a) I = 2 A (b) I = 10 A (see online version for colours)
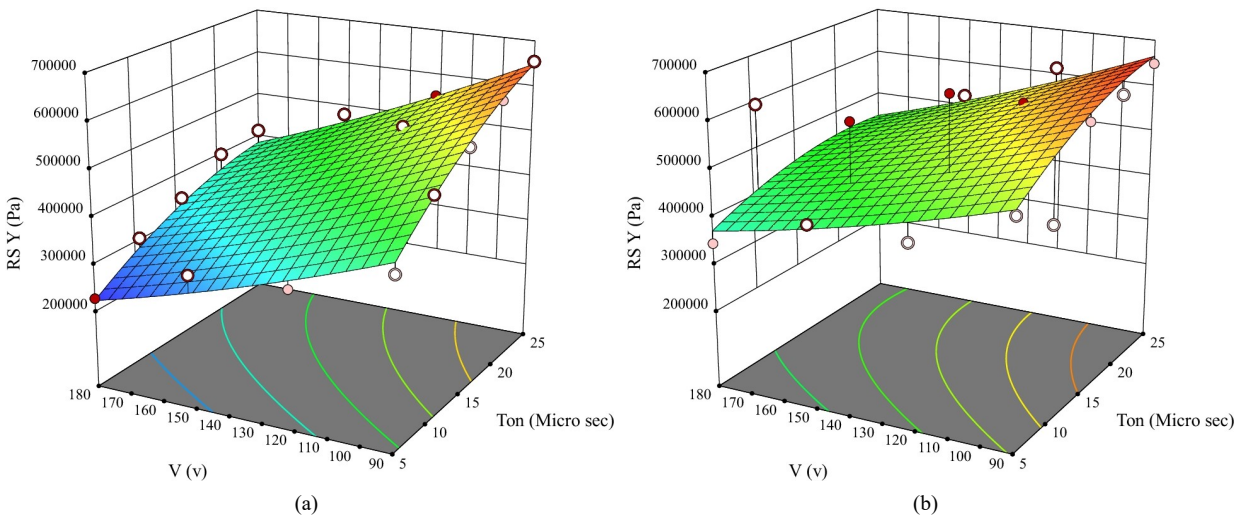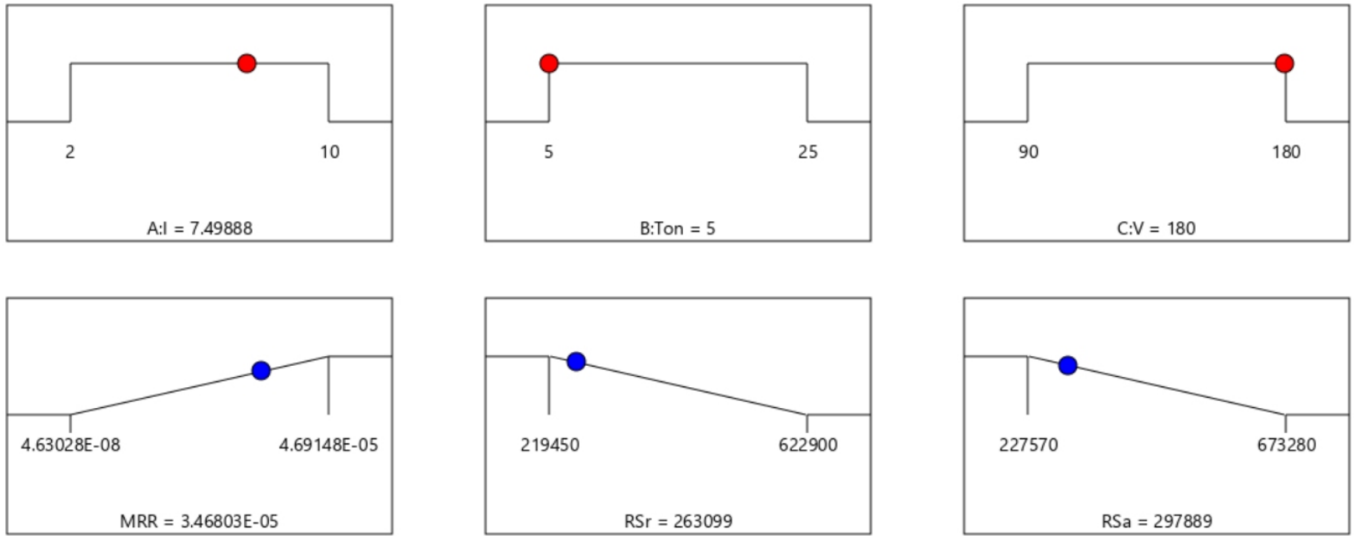

(a)

(b)

Figure 16 Optimised results (see online version for colours)

Notes: Desirability = 0.822; solution 1 out of 60.

Table 3 Fit statistics axial residual stresses

Std. dev.	47,179.41	R^2	0.8368
Mean	4.55E+05	Adjusted R^2	0.8205
CV%	10.38	Predicted R^2	0.799
		Adeq. precision	29.628

4.3 Effect of process parameters on MRR and residual stresses

Figure 7 is a 3D graph which depicts the effect of I and T_{on} on MRR, at different values of V, Figure 7(a) shows the variation at V = 90 V and Figure 7(b) shows the variation at V = 180 V. Figure 8 depicts the effect of I and V on MRR, at T_{on} = 5 μsec and T_{on} = 25 μsec [Figure 8(b)]. Figure 9 depicts the effect of T_{on} and V on MRR, at I = 2 A [Figure 9(a)] and I = 10 A [Figure 9(b)]. It can be observed that the MRR increases with increase in I and V, which can be explained as the power is product of I and V, hence by increasing I or V creates a powerful spark, which raises the temperature and causes more material to melt, but MRR decreases with increase in T_{on} as the value of PFE also follow the same.

Figure 10 is a 3D graph which depicts the effect of I and T_{on} on RS_r, at different values of V, Figure 10(a) shows the variation at V = 90 V and Figure 10(b) shows the variation at V = 180 V. Figure 11 depicts the effect of I and V on RS_r, at T_{on} = 5 μsec [Figure 11(a)] and T_{on} = 25 μsec [Figure 11(b)]. Figure 12 depicts the effect of T_{on} and V on RS_r, at I = 2 A [Figure 12(a)] and I = 10 A [Figure 12(b)]. It was observed that the value of RS_r firstly decreases and then increases by increasing the I value, and by increasing the T_{on} the RS_r value increases and by increasing V the RS_r decreases back.

Figure 13 is a 3D graph which depicts the effect of I and T_{on} on RS_a, at different values of V, Figure 13(a)

shows the variation at V = 90 V and Figure 13(b) shows the variation at V = 180 V. Figure 14 depicts the effect of I and V on RS_a, at T_{on} = 5 μsec [Figure 14(a)] and T_{on} = 25 μsec [Figure 14(b)]. Figure 15 depicts the effect of T_{on} and V on RS_a, at I = 2 A [Figure 15(a)] and I = 10 A [Figure 15(b)]. It can be observed that the value of RS_a decreases by increasing I and V, and it increases by increasing T_{on}.

When all objectives are allocated equal weightage, the combination of conditions with the highest desire function is chosen as the optimal condition, which is shown in Figure 16, which shows the optima values of MRR = 3.4688 × 10^{-5} m^3/sec, RS_r = 263,140 Pa and RS_a = 297,930 Pa, having desirability of 0.822 for I = 7.50053 A, T_{on} = 5.00002 μsec and V = 180 V were obtained, when equal weightage has been provided to all the objectives.

5 Conclusions

This research includes FEM and RSM for Ti-6Al-4V alloy EDM and investigates the influence of various machining input parameter combinations on output parameters and optimisation of the MRR, radial, and axial residual stresses created during machining. FEM is utilised for modelling and analysis, MRR and residual stress values are collected by simulation, and 100 sets of data are created from the FEM model and used for multi-objective optimisation using regression analysis. A quadratic model with Akaike's information criterion and backward selection was created using Design-Expert 13, and the data was analysed using ANOVA to evaluate the suitability of the constructed models. The ANOVA analysis and 3D surface plots shows that I, T_{on} and V have significant effect on MRR, RS_r, RS_a, As the ideal condition, the collection of conditions with the highest desire function is chosen, which is the optimal values of MRR = 3.4688 × 10^{-5} m^3/sec, RS_r

= 263,140 Pa and RS_a = 297,930 Pa, having desirability of 0.822 for I = 7.50053 A, T_{on} = 5.00002 μsec and V = 180 V were obtained, when equal weightage has been provided to all objectives. Furthermore, it was observed that the MRR improves with increasing the value of I and V, but drops by increasing the T_{on}, RS_a increases with increase in I and decreases with increase in T_{on} and V, and the RS_r initially decreases by increasing the I value but after a rise in the I value it increases, while its value first increases and then decreases with an increase in V. And the value of RS_r is directly proportional to T_{on}.

References

ANSYS, I. (2011) *ANSYS Mechanical APDL Element Reference*, ANSYS, Inc., USA.

Bhiradi, I., Raju, L. and Hiremath, S.S. (2019) 'Finite element modeling of single spark material removal and heat flux distribution in micro-electro discharge machining process', in *Advances in Manufacturing Technology*, pp.297–307, Springer, Singapore.

Boothroyd, G. and Winston, A.K. (1989) 'Non-conventional machining processes', in *Fundamentals of Machining and Machine Tools*, Marcel Dekker, Inc., New York, p.491.

Choubey, M., Maity, K. and Sharma, A. (2020) 'Finite element modeling of material removal rate in micro-EDM process with and without ultrasonic vibration', *Grey Systems: Theory and Application*, Grey Systems Laboratory.

Eubank, P.T., Patel, M.R., Barrufet, M.A. and Bozkurt, B. (1993) 'Theoretical models of the electrical discharge machining process. III. The variable mass, cylindrical plasma model', *Journal of Applied Physics*, Vol. 73, No. 11, pp.7900–7909.

Gu, L., Li, L., Zhao, W. and Rajurkar, K. (2012) 'Electrical discharge machining of Ti-6AL-4V with a bundled electrode', *International Journal of Machine Tools and Manufacturer*, Vol. 53, No. 1, pp.100–106.

Jaurker, D. and Pradhan, M. (2022) 'Process simulation of electrical discharge machining: a review', in *International Conference on Advances in Mechanical Engineering and Material Science*, Springer, pp.237–256.

Jithin, S., Bhandarkar, U.V. and Joshi, S.S. (2017) 'Analytical simulation of random textures generated in electrical discharge texturing', *Journal of Manufacturing Science and Engineering*, Vol. 139, No. 11.

Jithin, S., Bhandarkar, U.V. and Joshi, S.S. (2020) 'Multi-spark model for predicting surface roughness of electrical discharge textured surfaces', *The International Journal of Advanced Manufacturing Technology*, Vol. 106, No. 9, pp.3741–3758.

Joshi, S. and Pande, S. (2010) 'Thermo-physical modeling of die-sinking EDM process', *Journal of Manufacturing Processes*, Vol. 12, No. 1, pp.45–56.

Kansal, H., Singh, S. and Kumar, P. (2008) 'Numerical simulation of powder mixed electric discharge machining (PMEDM) using finite element method', *Mathematical and Computer Modelling*, Vol. 47, Nos. 11–12, pp.1217–1237.

Mhatre, M.S., Sapkal, S.U. and Pawade, R.S. (2014) 'Electro discharge machining characteristics of Ti-6Al-4V alloy: a grey relational optimization', *Procedia Materials Science*, Vol. 5.

Ming, W., Zhang, S., Zhang, G., Du, J., Ma, J., He, W., Cao, C. and Liu, K. (2022) 'Progress in modeling of electrical discharge machining process', *International Journal of Heat and Mass Transfer*, Vol. 187, p.122563.

Mohanty, C.P., Mahapatra, S.S. and Singh, M.R. (2017) 'Effect of deep cryogenic treatment on machinability of Inconel 718 in powder-mixed EDM', *International Journal of Machining and Machinability of Materials*, Vol. 19, No. 4, pp.343–373.

Nayak, R.K., Pradhan, M.K. and Sahoo, A.K. (2022) *Machining of Nanocomposites*, CRC Press, 6000 Broken Sound Parkway NW, Suite 300, Boca Raton, FL 33487-2742, 2 Park Square, Milton Park, Abingdon, Oxon, OX14 4RN.

Pradhan, B. and Bhattacharyya, B. (2009) 'Modelling of micro-electrodischarge machining during machining of titanium alloy Ti-6Al-4V using response surface methodology and artificial neural network algorithm', *Proceedings of the Institution of Mechanical Engineers, Part B: Journal of Engineering Manufacture*, Vol. 223, No. 6, pp.683–693.

Pradhan, M.K. and Biswas, C.K. (2008) 'Modeling of residual stresses of EDMed AISI 4140 steel', in *International Conference on Recent Advances in Materials, Processing and Characterization*, VRS Engineering College, Vijayawada, AP, India, pp.49–55.

Pradhan, M.K. and Biswas, C.K. (2008c) 'Neuro-fuzzy model on material removal rate in electrical discharge machining in AISI D2 steel', in *Proceedings of the 2nd International and 23rd All India Manufacturing Technology, Design and Research Conference*, Vol. 1, pp.469–474.

Pradhan, M. and Biswas, C. (2009) 'Neuro-fuzzy model and regression model a comparison study of MRR in electrical discharge machining of D2 tool steel', *Journal of Materials Processing Technology*, Vol. 209, No. 6, pp.2749–2755.

Pradhan, M.K. and Biswas, C.K. (2010) 'Neuro-fuzzy and neural network-based prediction of various responses in electrical discharge machining of AISI D2 steel: NF and NN based prediction of responses in EDM of D2 steel', *The International Journal of Advanced Manufacturing Technology*, Vol. 50, pp.591–610.

Pradhan, M.K. and Patel, R. (2020) in Sidpara, A.M. and Malayath, G. (Eds.): *Microelectro Discharge Machining: Principles and Applications*, Springer Nature Singapore Pte Ltd., Singapore.

Pradhan, M.K. et al. (2018) 'Optimisation of EDM process for MRR, TWR and radial overcut of D2 steel: a hybrid RSM-GRA and entropy weight-based topsis approach', *Int. J. Ind. Syst. Eng.*, Vol. 29, No. 3, p.273.

Pradhan, M.K. (2012) 'Determination of optimal parameters with multi response characteristics of EDM by response surface methodology, grey relational analysis and principal component analysis', *International Journal of Manufacturing Technology and Management*, Vol. 26, Nos. 1–4, pp.56–80.

Shastri, R.K. and Mohanty, C.P. (2022) 'A cost effective approach to explore the electrical discharge machined surface characteristics of nimonic C263 superalloy', *Journal of Materials Engineering and Performance*, Vol. 31, pp.9748–9767.

Tang, J. and Yang, X. (2018) 'Simulation investigation of thermal phase transformation and residual stress in single pulse EDM of Ti-6Al-4V', *Journal of Physics D: Applied Physics*, Vol. 51, No. 13, p.135308.

Yadava, V., Jain, V. and Dixit, P.M. (2004) 'Theoretical analysis of thermal stresses in electro-discharge diamond grinding', *Machining Science and Technology*, Vol. 8, No. 1, pp.119–140.